



# Physical connection between the tropical Indian Ocean tripole and western Tibetan Plateau surface air temperature during boreal summer

Mian Zhu<sup>1</sup> · Yazhou Zhang<sup>1,2</sup> · Jianping Li<sup>1,3</sup> · Ting Liu<sup>2,4</sup> · Zhaolu Hou<sup>1,3</sup> · Haili Wang<sup>5</sup>

Received: 21 May 2024 / Accepted: 20 August 2024

© The Author(s), under exclusive licence to Springer-Verlag GmbH Germany, part of Springer Nature 2024

## Abstract

This study investigated the influence of interannual variations in tropical Indian Ocean tripole (IOT) on the surface air temperature (SAT) over the western Tibetan Plateau (TP) during boreal summer. During the positive phase of the IOT, two northward cross-equatorial airflows are induced over the tropical eastern and western Indian Ocean. These airflows reinforce the ascending motion over the southern tropical Asia (15°–25°N, 80°–125°E), increasing local precipitation, as confirmed by observations and simulations by the Community Atmosphere Model. The upper-level Asian Continental Meridional Teleconnection (ACMT) pattern is excited by the latent heat released from precipitation and transmits signals from the southern tropical Asia to the western TP, leading to the positive geopotential height anomalies and anomalous anticyclones over there. Upper-level circulation anomalies over the western TP enhance atmospheric thickness through adiabatic processes, consequently elevating local SAT. The ACMT associated with precipitation anomalies thus serves as an atmospheric bridge connecting the IOT and the SAT variations over the western TP.

**Keywords** Indian Ocean tripole · Western Tibetan Plateau · Teleconnections · Surface air temperature

## 1 Introduction

The Tibetan Plateau (TP), often referred to as the ‘Roof of the World’, covers an area of 2.5 million km<sup>2</sup> at latitudes 26°–39°N and longitudes 73°–104°E, with an average elevation of ~4000 m. Its majestic mountain ranges, towering frost-covered peaks, and extensive glaciers make it the highest and most dramatic plateau on Earth. Due to the unique terrain of the TP, it absorbs solar radiation more intensely, resulting in surface air temperatures (SAT) that are higher compared to surrounding regions at similar latitudes. This heating affects eddies, waves and convective motions, thereby influencing the weather and climate of the plateau, as well as Asia and the Northern Hemisphere as a whole (Ye and Gao 1979; Yanai et al. 1992; Tao et al. 1999; Zhou et al. 2009; Zou et al. 2014; Li and Zhang 2021). For example, Wang et al. (2007) pointed out that in spring, the temperature of the TP is a more significant factor affecting its snow cover changes compared to precipitation. Huang (2003) found that the surface heating field of the TP in the preceding winter influences the 500 hPa geopotential height in the subsequent spring, leading to anomalous spring temperatures in the Sichuan-Chongqing region to the east of the

---

✉ Yazhou Zhang  
zyz@ouc.edu.cn

✉ Jianping Li  
ljp@ouc.edu.cn

<sup>1</sup> Frontiers Science Center for Deep Ocean Multispheres and Earth System (FDOMES)/Key Laboratory of Physical Oceanography/Academy of the Future Ocean/College of Oceanic and Atmospheric Science, Ocean University of China, Qingdao, China

<sup>2</sup> State Key Laboratory of Satellite Ocean Environment Dynamics, Second Institute of Oceanography, Ministry of Natural Resources, Hangzhou, China

<sup>3</sup> Laoshan Laboratory, Qingdao, China

<sup>4</sup> Southern Marine Science and Engineering Guangdong Laboratory (Zhuhai), Zhuhai, China

<sup>5</sup> State Key Laboratory of Tropical Oceanography, South China Sea Institute of Oceanology, Chinese Academy of Sciences, Guangzhou, China

plateau. Yu et al. (2005) revealed the impact of the surface temperature of the TP on changes in summer precipitation in North China. Further studies have also explored the influence of the thermal conditions of the TP on the Asian summer monsoon (Hu and Duan 2015; Son et al. 2020; Wang et al. 2018; Zhou et al. 2021). Therefore, understanding the driving factors behind temperature changes in the TP is crucial for enhancing our understanding of the plateau's impact on global climate.

Many studies have explored the influence of various climate modes on TP temperatures. The Arctic Oscillation (AO) is a key driver of winter climate patterns in the Northern Hemisphere, and previous studies have found a strong relationship between the AO and SAT over the TP, driven by changes in regional atmospheric circulation patterns associated with the AO (Jiao et al. 2014; Deng et al. 2024), although this may apply only in certain TP regions (Cuo et al. 2013; Deng et al. 2023). Furthermore, the North Atlantic Oscillation (NAO) is also an important climate mode influencing the temperature of the TP. One significant way in which the NAO impacts the temperature of the TP is through teleconnection (Si et al. 2023). For example, Li et al. (2008) pointed out that the NAO indirectly influences the North Atlantic–Ural–East Asia (NAULEA) teleconnection, which in turn affects cloud formation over the TP, thereby influencing its temperature. Further studies indicate that NAO tends to lower spring temperatures on the TP, primarily due to its influence on the jet stream (Li et al. 2005; Liu et al. 2018b; Li et al. 2021). Moreover, it is well established that sea surface temperature anomalies (SSTA) over the tropical Pacific Ocean, particularly El Niño–Southern Oscillation (ENSO), affect temperature conditions over the TP. The influence of the ENSO on the temperature of the TP is complex. Eastern Pacific El Niño events lead to more frequent extreme cold events on the TP, while Central Pacific El Niño events have a weaker impact on extreme temperatures (Yong et al. 2023). Yin et al. (2000) conducted a regional study of the TP and found that concurrent ENSO events affect temperatures in the northeast and southeast parts of TP. Jiang et al. (2019) revealed that during the positive phases of ENSO, suppressed convection in the western North Pacific Ocean can lead to non-adiabatic cooling, which may induce strong cold anomalies in the eastern TP. Additionally, Bafitlhile and Liu (2023) focused more on the impact of ENSO on the southern TP.

Previous studies on this topic have focused on the effects of climate variability over the Pacific, Atlantic, and Arctic oceans and Eurasia on TP temperature variability. The Indian Ocean lies to the south of the TP and, as the nearest ocean, exerts a significant influence on TP climate evolution. There are two dominant interannual modes in the Indian Ocean, the Indian Ocean basin (IOB) mode and Indian Ocean dipole (IOD), both of which have significant impacts

on climate change over the TP. Zhao et al. (2018) pointed out that during the positive phase of the IOB, the local Hadley circulation is enhanced, altering the thermal forcing over the TP in May. Zhang et al. (2022a) found that the IOB and tropical North Atlantic SSTA jointly affect late summer TP precipitation in August. Li et al. (2022a) suggested that the IOB might be a major factor controlling the interannual variability of summer temperatures over the TP. Li et al. (2017) indicated that changes in monsoon precipitation in southeastern TP might be driven by the IOD on the multi-centennial scale. Zhang and Duan (2023) stated that the IOD influences TP precipitation by regulating the moisture circulation over the tropical Indian Ocean and the subtropical northwestern Pacific. Zhang et al. (2019) further suggested that the IOD significantly affects TP precipitation by influencing the anticyclonic anomalies over the Indian subcontinent and the Bay of Bengal, as well as the westerly jet over the North Atlantic, thereby modulating moisture transport over the Indian subcontinent and Central Asia. Additionally, Li and Zhang (2023) believed that changes in the IOD could alter low-level winds over the TP, thus impacting precipitation. However, these studies predominantly focused on the impact of the Indian Ocean on precipitation over the TP, and paid less attention to the temperature.

The evolution characteristics of IOD are complex. Du et al. (2013) divided IOD events into three types according to different temporal evolution characteristics of IOD events. Endo and Tozuka (2016) divided IOD events into canonical IOD and "IOD Modoki" according to their different spatial characteristics. Subsequently, Tozuka et al. (2016) further investigated the significant differences in the anomalous Walker circulation between these two types of IOD. Zhang et al. (2020) pointed out that IOD Modoki is actually the third leading mode (EOF3) of SSTA in the Indian Ocean and named it IOT. Subsequent studies on atmospheric and oceanic processes demonstrated that the IOT exists independently of the IOD (Zhang et al. 2020). The independent climatic effects of the IOT on summer SAT in the western United States, and on summer extreme low temperatures in central Siberia have also been studied (Zhang et al. 2022a, b). According to the coupled oceanic–atmospheric bridge theory (Li et al. 2019), the upper-level Asian Continental Meridional Teleconnection (ACMT) serves as an atmospheric bridge for the IOT to affect central Siberia (Zhang et al. 2022b). The ACMT also passes by the western TP, leading us to consider the possibility of a connection between the IOT and climate change over the western TP.

The rest of this article is organized as follows. Section 2 provides a detailed introduction to the datasets and methods, while Sect. 3 explores the relationship between IOT and SAT over the western TP. In Sect. 4, we investigate the underlying physical mechanism of the IOT effects on the SAT over the western TP during boreal summer (June–July–August,

JJA), including the effect of the circulation anomalies related to IOT over the western TP on local SAT and the linkage between IOT and circulation anomalies over the western TP. Atmospheric processes related to the impact of the IOT on SAT were validated using the Community Atmosphere Model version 5 (CAM5) in Sect. 5, and the conclusion and discussion are presented in Sect. 6.

## 2 Datasets, indices, methods, and numerical experiments

### 2.1 Datasets

The following datasets were employed in this study for the period 1982–2022.

1. Monthly oceanic SST data ( $1.0^\circ \times 1.0^\circ$  horizontal resolution) were derived from the Optimum Interpolation SST (OISST; Reynolds et al. 2002). The improved Extended Reconstructed SST version 5 (ERSST v5; Huang et al. 2017) dataset ( $2^\circ \times 2^\circ$  horizontal resolution) was used to verify results.
2. Monthly atmospheric variables including geopotential height (HGT), zonal, and meridional winds (with 10 levels from 1000 to 200 hPa), atmosphere thickness, total cloud cover and downward solar radiation flux were obtained from two separate datasets: (a) the National Centers for Environmental Prediction reanalysis (NCEP2), with a  $2.5^\circ \times 2.5^\circ$  grid (Kanamitsu et al. 2002; <https://psl.noaa.gov/data/gridded/data.ncep.reanalysis2.html>), and (b) the European Centre for Medium-Range Weather Forecasts (ECMWF) Reanalysis version 5 (ERA5), with a  $0.25^\circ \times 0.25^\circ$  grid (Hersbach et al. 2020; <https://www.ecmwf.int/en/forecasts/datasets/reanalysisdatasets/era5>).
3. Two SAT datasets were employed, from the Global Historical Climatology Network (GHCN) dataset with a  $0.5^\circ \times 0.5^\circ$  grid (Menne et al. 2012; <https://www.psl.noaa.gov/data/gridded/data.ghcncams.html>) and the Berkeley Earth Surface Temperature (BEST) dataset with a  $1^\circ \times 1^\circ$  grid (Rohde et al. 2013a, b; <https://berkeleyearth.org/data>).
4. The study also used two precipitation datasets, one from the Climate Prediction Center Merged Analysis of Precipitation (CMAP; Xie and Arkin 1997), and another one from the Global Precipitation Climatology Project (GPCP; Huffman et al. 2015), with a  $2.5^\circ \times 2.5^\circ$  grid.

### 2.2 Indices

Zhang et al. (2020) indicates that the IOT can be identified as the EOF3 pattern (passed the *North's* test), which

explains  $\sim 7\%$  of the total variance of the tropical Indian Ocean SSTA (Fig. 1a, c). We applied the IOT mode index (TMI) defined by Zhang et al. (2020), which represents the difference in SSTA between the tropical central ( $5^\circ\text{--}20^\circ\text{S}$ ,  $65^\circ\text{--}85^\circ\text{E}$ ) and southeastern ( $10^\circ\text{S--}0^\circ$ ,  $90^\circ\text{--}110^\circ\text{E}$ ) and western ( $5^\circ\text{S--}20^\circ\text{N}$ ,  $45^\circ\text{--}60^\circ\text{E}$  and  $10^\circ\text{--}20^\circ\text{N}$ ,  $60^\circ\text{--}70^\circ\text{E}$ ) sectors of the Indian Ocean (Fig. 1a, c). The TMI exhibits the highest correlations with the third principal component (PC3), with values of 0.88 and 0.81 when using the OISST and ERSST datasets (Fig. 1b, d), respectively. This indicates that this index is thus effective for representing IOT variability (Zhang et al. 2020). According to Zhang et al. (2020), the IOT has strong seasonality and peaks in JJA, so we select the JJA index of IOT as the forcing factor.

### 2.3 Methods

The significance of correlations between variables  $X$  and  $Y$  was tested with a two-tailed Student's  $t$  test using the effective number of degrees of freedom ( $N_{eff}$ ), as given in the following approximation (e.g. Bretherton et al. 1999; Li et al. 2013):

$$\frac{1}{N_{eff}} \approx \frac{1}{N} + \frac{2}{N} \sum_{i=1}^N \frac{N-i}{N} \rho_{XX}(i) \rho_{YY}(i),$$

where  $N$  is the total number of samples in the time series; and  $\rho_{XX}(i)$  and  $\rho_{YY}(i)$  denote the autocorrelations of the two time-series  $X$  and  $Y$  at time lag  $i$ , respectively.

To determine if tropical southern Asia can trigger Rossby waves, the Rossby wave source (RWS) is calculated at 200 hPa following Sardeshmukh and Hoskins (1988):

$$RWS = -\nabla \cdot (f + \zeta) V_\chi = -(f + \zeta) D - V_\chi \cdot \nabla (f + \zeta),$$

where the RWS represents Rossby wave source. The  $f$  and  $\zeta$  are planetary vorticity and relative vorticity, respectively.  $D$  represents the horizontal divergence and  $V_\chi$  represents the divergent component of the horizontal wind.

Rossby wave ray tracing theory in horizontally nonuniform basic flows was used to track the trajectory of stationary Rossby wave trains and delineate the pathway of the influence of heat sources in the southern tropical Asia (Li and Li 2012; Li et al. 2015; Zhao et al. 2015, 2019). Previous studies have shown that the dispersion relationship between Rossby wave frequency and wavenumber in horizontally non-uniform flows can be formulated as follows (Karoly 1983; Li and Nathan 1997; Li and Li 2012; Li et al. 2015; Zhao et al. 2015, 2019):

$$\omega = \bar{u}_M k + \bar{v}_M k + \frac{\bar{q}_x l - \bar{q}_y k}{k^2 + l^2}, \quad (1)$$

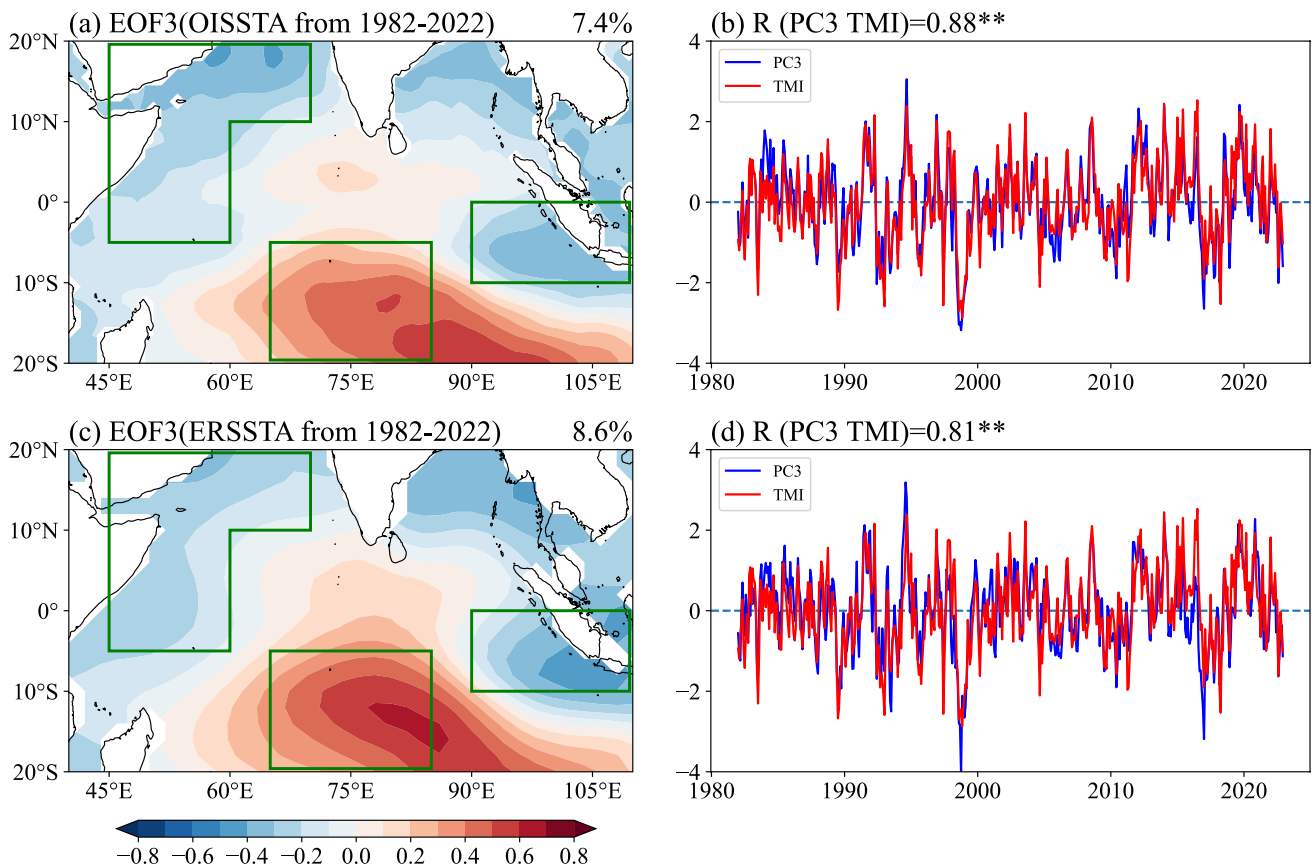


**Fig. 1** **a** Spatial patterns of the EOF3 of the monthly SSTA over the tropical Indian Ocean based on the OISST dataset. The value at the upper right is the explained variance. The three green boxes respectively denote the central tropical (5°–20°S, 65°–85°E), southeastern (10°S–0°, 90°–110°E) and western (5°S–20°N, 45°–60°E and 10°–20°N, 60°–70°E) sectors of the Indian Ocean. **b** Normalized time

series of the monthly third principal component (PC3; blue) and TMI (red) from the OISST dataset for the period 1982–2022. The correlation coefficient (R) between the PC3 and TMI is 0.88 at >99% confidence level. **c** As in (a), but for the ERSST dataset. **d** As in (b), but for the ERSST dataset and R=0.81 at >99% confidence level

where  $\omega$  is the wave frequency;  $k$  and  $l$  are the zonal and meridional wavenumbers, respectively;  $(\bar{u}_M, \bar{v}_M) = (\bar{u}, \bar{v})/\cos\varphi$  is the Mercator projection of zonal and meridional winds;  $\varphi$  is the latitude;  $\bar{q} = \nabla_M^2 \bar{\psi} / \cos^2\varphi + f$  represents the absolute vorticity of the background; and  $\bar{q}_x$  and  $\bar{q}_y$  are the zonal and meridional gradients of  $\bar{q}$ , respectively. The total wavenumber is represented by  $K = \sqrt{k^2 + l^2}$ , and zonal and meridional components of the group velocity are as follows:

$$u_g = \frac{\partial\omega}{\partial k} = \bar{u}_M + \frac{(k^2 - l^2)\bar{q}_y - 2kl\bar{q}_x}{K^4}, \tag{2a}$$

$$v_g = \frac{\partial\omega}{\partial l} = \bar{v}_M + \frac{(k^2 - l^2)\bar{q}_x - 2kl\bar{q}_y}{K^4}. \tag{2b}$$

When the background flow varies along the ray, wavenumbers determined by the kinematic wave theory (Whitham 1960) can be expressed as follows:

$$\frac{d_g k}{dt} = -\frac{\partial\omega}{\partial x} = -k \frac{\partial\bar{u}_M}{\partial x} - l \frac{\partial\bar{v}_M}{\partial x} - \frac{1}{K^2} \left( l \frac{\partial\bar{q}_x}{\partial x} - k \frac{\partial\bar{q}_y}{\partial x} \right), \tag{3a}$$

$$\frac{d_g l}{dt} = -\frac{\partial\omega}{\partial y} = -k \frac{\partial\bar{u}_M}{\partial y} - l \frac{\partial\bar{v}_M}{\partial y} - \frac{1}{K^2} \left( l \frac{\partial\bar{q}_x}{\partial y} - k \frac{\partial\bar{q}_y}{\partial y} \right), \tag{3b}$$

where  $\frac{d_g}{dt} = \frac{\partial}{\partial t} + \bar{u}_g \frac{\partial}{\partial x} + \bar{v}_g \frac{\partial}{\partial y}$  represents the material derivative moving with the group velocity. In Eqs. (3a, 3b), both zonal and meridional wavenumbers vary along the wave ray, which is a departure from classical theory (Hoskins and Karoly 1981). Termed as the wave ray tracing equation set, Eqs. (2a, 2b) and (3a, 3b) allow determination of the initial local meridional wavenumber  $l$  after providing the initial position and zonal wavenumber,  $k$ , as in Eq. (1). Subsequently, the wave ray tracing equation set facilitates the derivation of the corresponding wave ray trajectory. For large-scale Rossby waves, integration ceases when the local

meridional wavelength falls below 1000 km (Wang et al. 2022, 2023).

We used the perturbation hypsometric equation (Sun et al. 2016; Li et al. 2022b) as follows to examine the impact of atmospheric circulation variability on air temperature:

$$T' = \frac{g_0}{R} \left( \ln \frac{p_1}{p_2} \right)^{-1} \Delta Z', \quad (4)$$

where  $\langle T' \rangle$  and  $\Delta Z'$  represent the anomalies or deviations from their temporal averages between two pressure surfaces  $p_1$  and  $p_2$ , respectively;  $g_0$  denotes the acceleration due to gravity, and  $R$  stands for the gas constant of dry air. Based on Eq. (4), the perturbation mean air temperature within the atmospheric layer is directly related to the perturbation atmospheric thickness delimited by isobaric surfaces. The anomaly in atmospheric thickness thus serves as a proxy for the perturbation mean air temperature of the atmospheric layer. A decrease in atmospheric thickness corresponds to a reduction in the mean air temperature of the atmospheric layer; Conversely, an increase in thickness correlates with a rise in temperature. We employed this perturbation hypsometric equation to explore the impact of upper-level atmospheric circulation on air temperature anomalies.

## 2.4 Numerical experiments

In Sect. 4.2, we show that precipitation in the southern tropical Asia is a key link for IOT to affect the SAT of the western TP. To verify the influence of the IOT on precipitation over the southern tropical Asia (15°–25°N, 80°–125°E), we conducted numerical experiments using the CAM5 model, which uses a horizontal grid with a resolution of approximately 1.9° × 2.5° and 26 hybrid sigma-pressure levels (available at [http://www.cesm.ucar.edu/models/cesm1.0/cam/docs/description/cam5\\_desc.pdf](http://www.cesm.ucar.edu/models/cesm1.0/cam/docs/description/cam5_desc.pdf)). CAM5 has been widely used in studies of atmospheric circulation responses to external forcings (i.e., SST and sea-ice, Meehl et al. 2012; He and Wu 2014).

Here, we designed two CAM5 experiments with different lower boundary conditions: a control run, and a positive IOT forcing sensitivity experiment, which is shown in Table 1.

The control run was forced by monthly climatological SST globally over 1982–2011. The positive IOT forcing was driven by the climatological SST plus the SSTA related to positive IOT events, with the positive SSTA over the tropical central (5°–20°S, 65°–85°E) and the negative SSTA over the tropical southeastern (10°S–0°, 90°–110°E) and western (5°S–20°N, 45°–60°E and 10°–20°N, 60°–70°E) Indian Ocean, and climatological SST are imposed in remaining regions. Notably, these SSTA in the tropical Indian Ocean were extracted from positive IOT events in 1991, 1994, 2003, 2008, and 2016 (Zhang et al. 2020), and were linearly added to the climatological SST in the tropical Indian Ocean. Both experiments were simulated for 33 years, the first 3 years are used as the initial adaptation period, and the remaining simulation results are used to analyze. The forcing boundaries in the sensitive experiment was not treated. But we verified that the model closely matches the observed spatial patterns of precipitation and winds climatology (not shown). This suggests that untreated boundary forcing has a minor impact on the simulation results. It should be noted that we used the same numerical experiment as Zhang et al. (2022b).

## 3 Spatiotemporal relationship between the IOT and SAT over the western TP

Figure 2 displays the spatiotemporal relationship between the IOT and SAT over the western TP. The significant positive correlations both on spatial and temporal levels between the IOT and SAT are clearly observed over the western TP based on the GHCN data (Fig. 2a, b), and the correlation between the IOT and area-averaged SAT anomalies over the western TP (35°–45°N, 75°–90°E) is 0.44 at > 99% confidence level (Fig. 2b). This suggests that during the positive phase of the IOT, the SAT over the western TP increases. These significant results can also be obtained using the BEST data (Fig. 2c, d). These preliminary correlation analyses indicate that the IOT is intrinsically linked to SAT over the western TP during JJA. Furthermore, there was a strongly negative correlation zone in northern parts

**Table 1** The detailed information of the CAM5 experiments in this study

Numerical experiments	Detailed settings of the experiments
Control run	A 30-year integration with climatological SST prescribed as the lower boundary condition in the global oceanic domain
Positive IOT forcing	The positive SSTA are specified in the tropical central (5°–20°S, 65°–85°E) and the negative SSTA are specified in the tropical southeastern (10°S–0°, 90°–110°E) and western (5°S–20°N, 45°–60°E and 10°–20°N, 60°–70°E) Indian Ocean, and climatological SST are imposed in other regions

Note that, for the positive IOT forcing case, the SST forcing is extracted in the tropical Indian Ocean (20°S–20°N, 40°–110°E) based on the positive IOT years



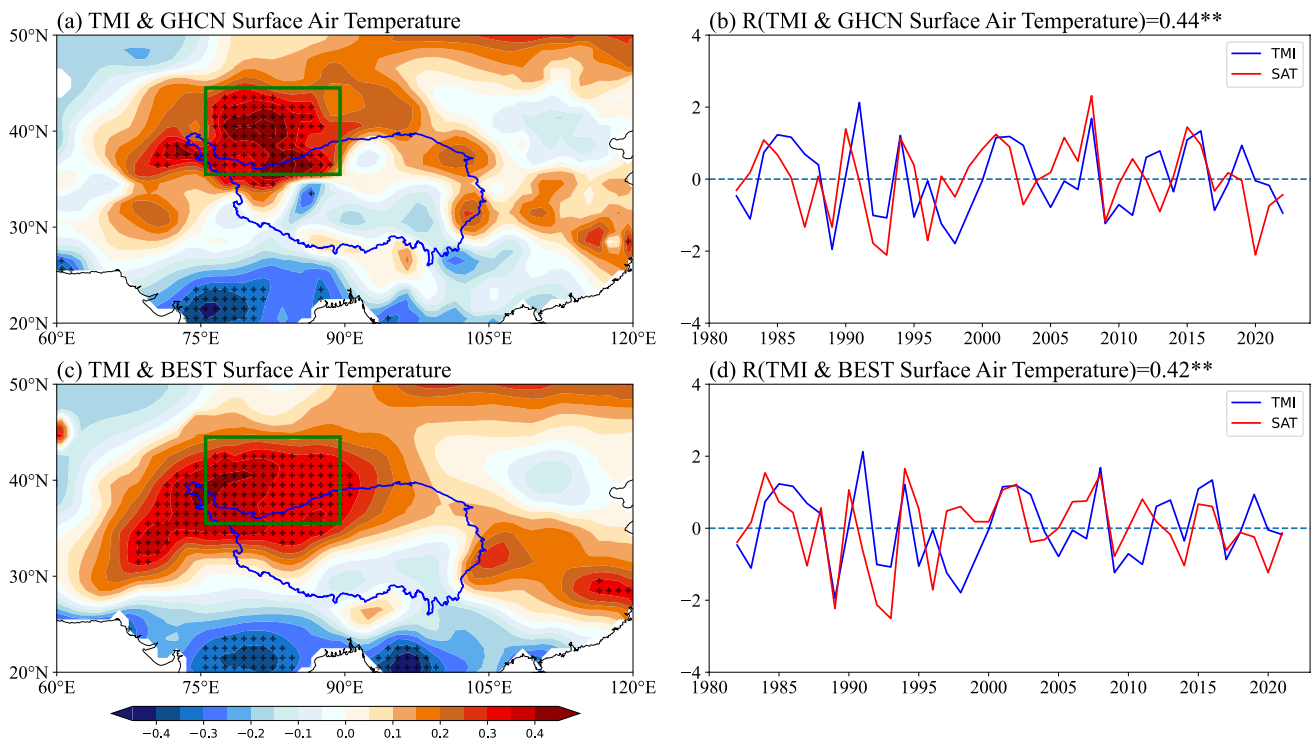


**Fig. 2** **a** Correlation map between the TMI and SAT during JJA based on the GHCN data. The green box denotes the western TP region (35°–45°N, 75°–90°E). The blue contour represents the outline of the TP. The black stippled areas indicate the significant correlations above the 95% confidence level. **b** Time series of the TMI (blue) and

area-averaged SAT (red) over the western TP (the green box in **a**) from the GHCN data. Correlation between the two time-series is significant above the 99% confidence level. **c** As in **a**), but for the BEST data. **d** As in **b**), but for the BEST data

of the Indian and Indochinese peninsulas, but this was not investigated here. Because ENSO is highly correlated with IOB and IOB, IOD, and IOT are orthogonal, the preceding and simultaneous ENSO, IOB and IOD signals are not significantly related to IOT. They hardly affect the relationship between IOT and the SAT over the western TP. This is also confirmed by the results obtained using partial correlation to remove the ENSO, IOB and IOD signals (not shown). Possible mechanisms that drive the effects of the IOT on SAT over the western TP were investigated as follows.

## 4 Potential physical mechanisms

### 4.1 Effect of the circulation anomalies related to IOT over the western TP on local SAT

Changes in SAT are usually strongly linked to variations in atmospheric circulation. Figure 3 presents the spatial correlations between the IOT and 200 hPa geopotential height and wind anomalies during JJA, based on the NCEP2 and ERA5 datasets. As shown in Fig. 3, over the western TP, there is a significant positive correlation region, accompanied by an anticyclonic circulation. These imply that when positive IOT

events mature during JJA, the significant positive anomalies in geopotential height develop over the western TP and are accompanied by the strong anomalous anticyclone (Fig. 3). Such anomalous circulation patterns favor the development of the subsidence movement. To verify this result, Fig. 4 displays the meridional-vertical distribution of the omega and wind anomalies associated with the IOT. The remarkable positive omega anomalies occur over the western TP, suggesting the enhancement of the subsidence movement (Fig. 4).

Previous studies have reported that upper-level atmospheric circulation over middle–high-latitude land masses is relatively insensitive to local surface warming/cooling (Screen et al. 2012; Tang et al. 2013). Upper-level atmospheric circulation may therefore impact SAT changes through adiabatic expansion/compression. The anomalous high or low is respectively linked to higher or lower geopotential height, leading to warmer or cooler local SAT (Sun et al. 2016; Li et al. 2022b).

The spatial correlation between the IOT and atmospheric thicknesses anomalies at 500–200 hPa during JJA is shown in Fig. 5, based on the NCEP2 and ERA5 datasets. There is clearly a significant positive correlation over the western TP. This means that the positive geopotential height anomalies

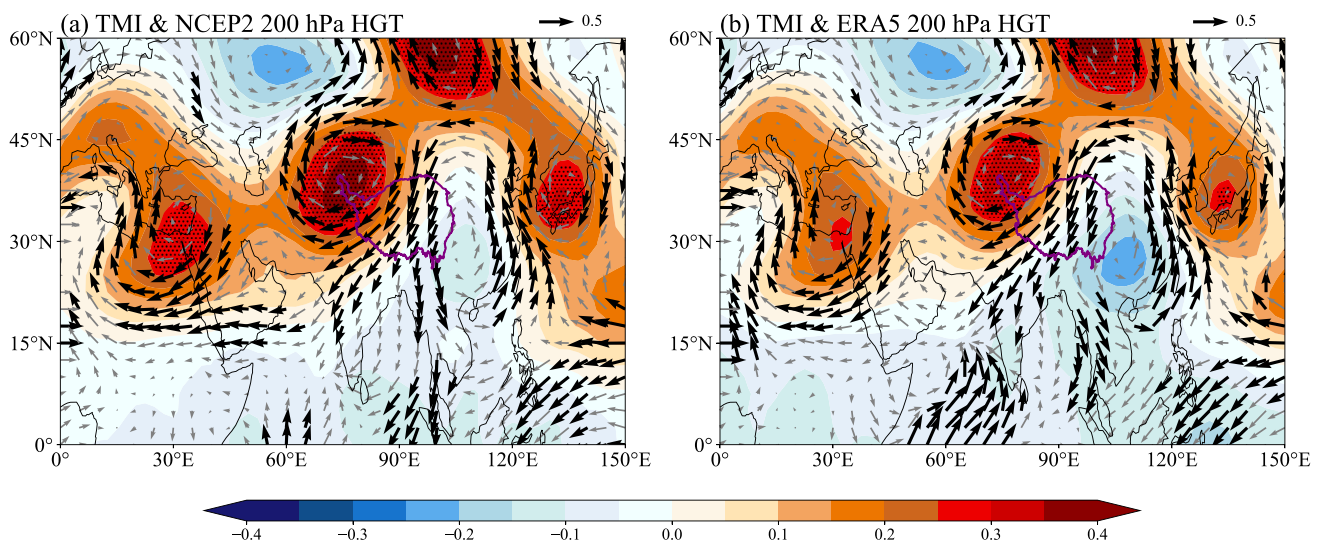


**Fig. 3** **a** Correlation map of the TMI with the geopotential height (HGT, shading) and wind anomalies (vector) at 200 hPa during JJA based on the NCEP2 dataset. The purple contour represents the out-

line of the TP. The black vectors and the black stippled areas indicate the significance above the 95% confidence level. **b** As in (a), but using the ERA5 dataset

in that region favor an increase in middle–upper-level tropospheric (500–200 hPa) atmosphere thickness (Fig. 5), driving a thickening of the atmospheric boundary layer and promoting warmer than normal SAT through modulation of adiabatic expansion/compression (Fig. 2). Furthermore, the anomalous circulation over the western TP may not only change local atmospheric thickness, but also local total cloud cover, affecting the intensity of shortwave solar radiation reaching the ground (not shown). However, the results are not significant, primarily considering that this is not the main factor causing the SAT increase.

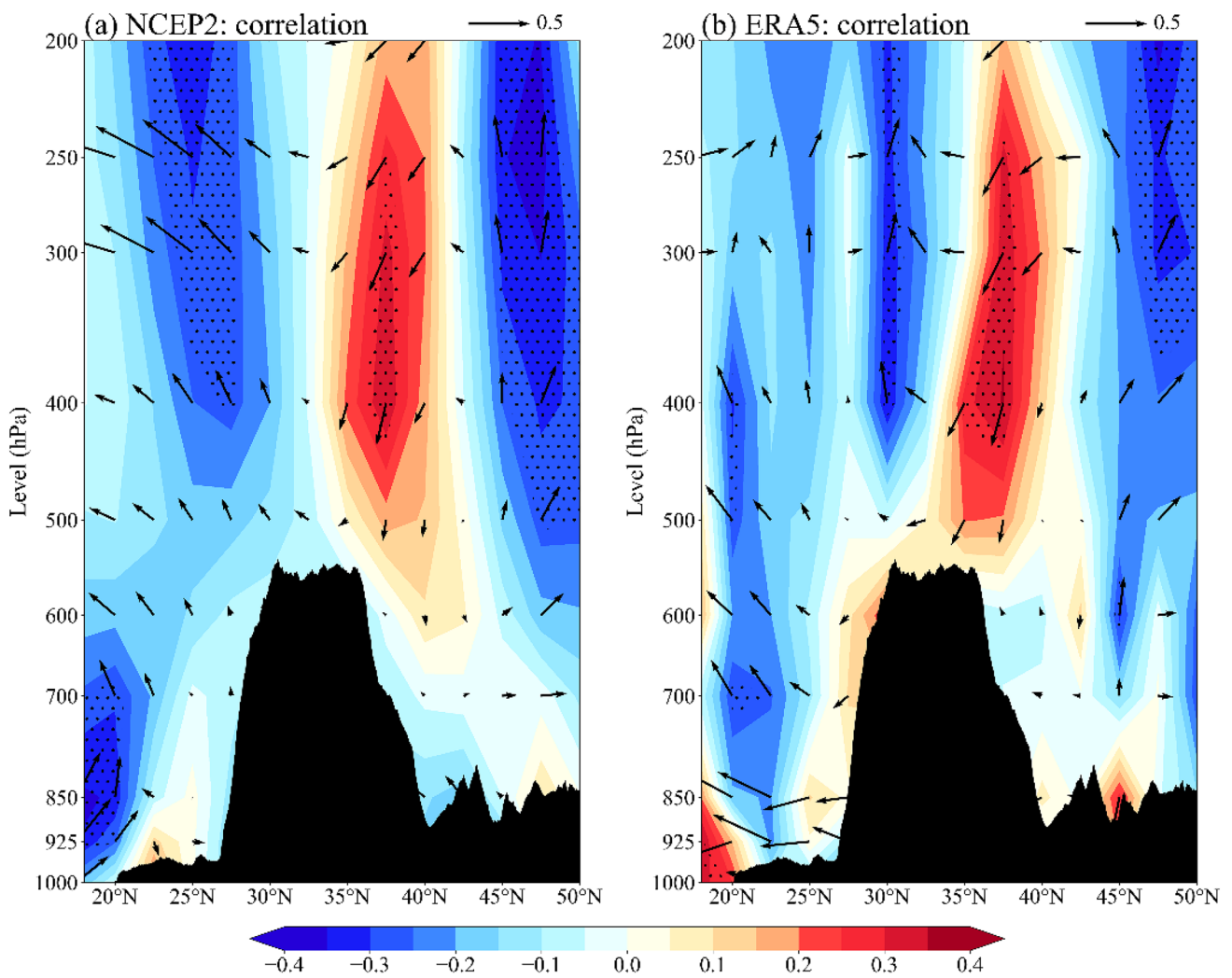
Overall, we have established the effect of the circulation anomalies related to IOT over the western TP on local SAT. During the positive IOT phase, the western TP experiences elevated geopotential height anomalies and anomalous anticyclonic circulation. This induces anomalous subsidence movement over the TP, altering atmospheric thickness and influencing solar radiation influx, ultimately contributing to SAT elevation.

#### 4.2 Linkage between IOT and circulation anomalies over the western TP

The mechanism by which the IOT affects western TP circulation anomalies was considered further. The atmospheric bridge is a key physical process through which tropical ocean modes influence extratropical climate variability (Li et al. 2019). Previous studies have pointed out that the IOT-related teleconnections, such as circumglobal teleconnection (CGT)-like pattern (Ding and Wang 2005) and ACMT, are the atmospheric bridges that IOT affects the western United States and central Siberia, respectively, and these

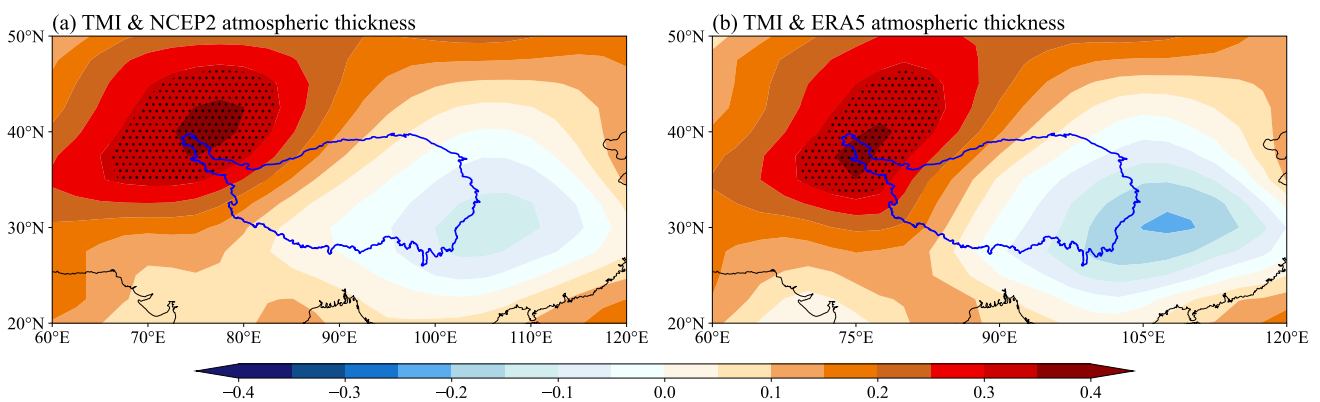
two atmospheric bridges are stimulated by the precipitation in the southern tropical Asia (Zhang et al. 2022a, b), so the precipitation in tropical South Asia and the atmospheric teleconnections caused by precipitation are the key atmospheric bridges for IOT to affect extratropical climate variability. We hypothesize that precipitation in the southern tropical Asia is a key link for IOT to affect the SAT over the western TP.

Figure 6a, b shows the relationship between the IOT and precipitation, together with 850 hPa wind over the tropical Indian Ocean and western Pacific Ocean (20°S–40°N, 40°–160°E). In the figure, there is a significant cyclonic circulation in the central tropical Indian Ocean, and significant anticyclonic circulations exist in the eastern and western tropical Indian Ocean, respectively. These two anticyclonic circulations cross the equator and converge in the southern tropical Asia. The precipitation field exhibits a spatial distribution pattern similar to that of the IOT, with a significant positive correlation in the central tropical Indian Ocean and negative correlations in the eastern and western tropical Indian Ocean. Significant positive correlations also appear in the southern tropical Asia, indicating an excess of precipitation associated with the IOT (Fig. 6a, b). Surplus precipitation is attributed mainly to negative precipitation anomalies corresponding to anomalous anticyclones over the tropical eastern and western tropical Indian Ocean, particularly in the Arabian Sea area (Fig. 6a, b). Such anomalies favor the formation of anomalous cross-equatorial winds off the coasts of East Africa and Sumatra/Java coasts (Fig. 6a, b). On the western side of the anticyclonic activity, near the Sumatra/Java coast, intensified southerly anomalies tend to reinforce anomalous cyclonic activity over the tropical central southern Indian Ocean. The enhanced cyclonic activity



**Fig. 4 a** Correlations of the TMI with the meridional-vertical circulation anomalies (vectors) and omega (shading) averaged over 65°–95°E during JJA based on the NCEP2 dataset. When plotting the

shading, the negative values of omega were used. The black stippled areas indicate significance above the 90% confidence level. **b** As in (a), but using the ERA5 dataset



**Fig. 5 a** Correlations between the TMI and the 500–200 hPa atmospheric thickness during JJA based on the NCEP2 dataset. The blue contour represents the outline of the TP. The black stippled areas

indicate the significant correlations above the 95% confidence level. **b** As in (a), but using the ERA5 dataset



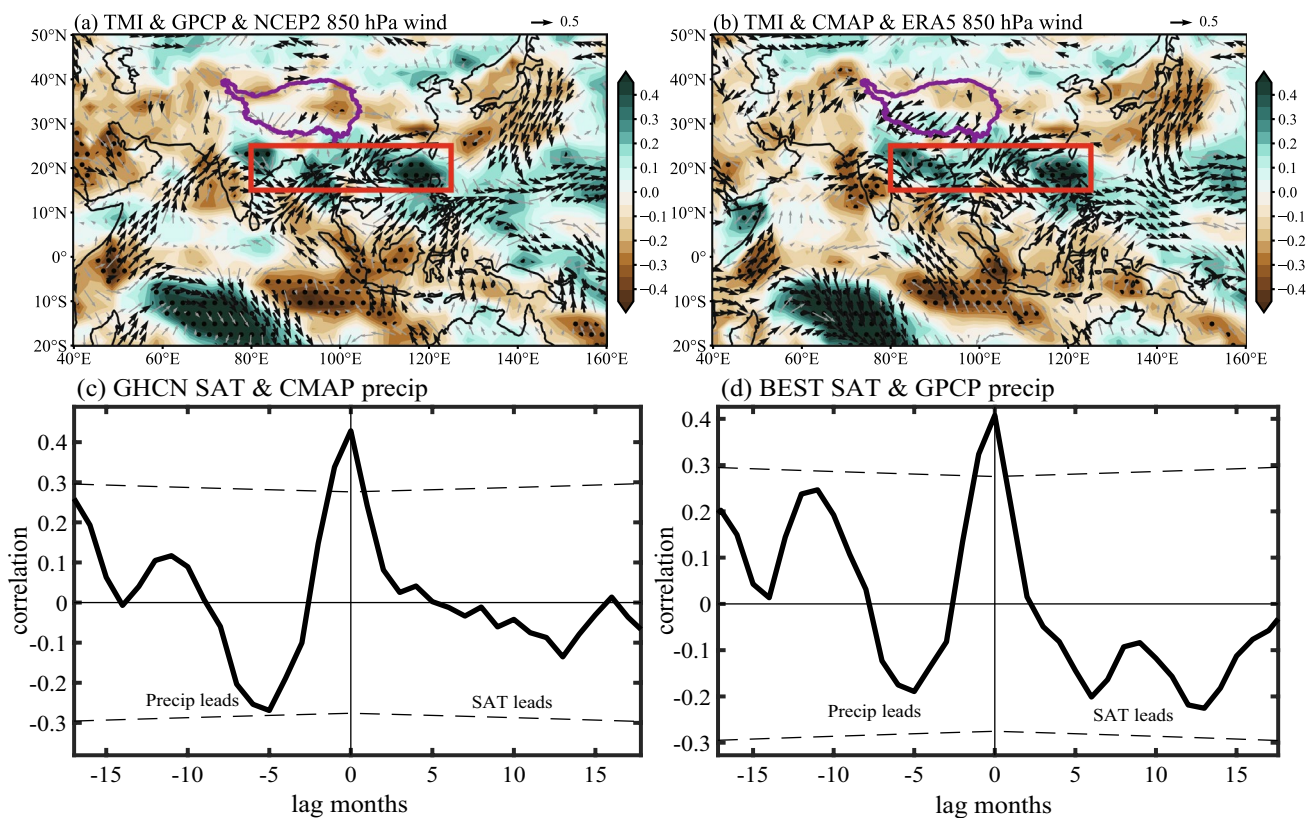


**Fig. 6** **a** Correlations of the TMI with precipitation (shading) and 850 hPa wind anomalies (vector) during JJA based on the GPCP and NCEP2 datasets. The purple contour represents the outline of the TP. The red box denotes the southern tropical Asia region. The black vectors and the black stippled areas indicate the significant values above the 90% confidence level. **c** Lead-lag correlations of the area-

averaged SAT anomalies over the western TP with the area-averaged precipitation anomalies in the southern tropical Asia based on the GHCN and CMAP datasets. The dashed line indicates the 95% confidence level. **b** As in (a), but for the CMAP and ERA5 datasets. **d** As in (c), but for the BEST and GPCP datasets

further strengthens the cross-equatorial winds off the East African coast (Fig. 6a, b). These two robust cross-equatorial airflows develop in the tropical eastern and western Indian Ocean, transitioning into westerly anomalies over the northern Indian Ocean, together with the anomalous east airflow from the western Pacific Ocean, transporting additional moisture to the southern tropical Asia, where they converge. This convergence enhances the ascending motion, contributing to excessive local precipitation (Fig. 6a, b; Zhang et al. 2022a, b).

Correspondingly, the surplus precipitation serves as a heat source through the latent-heat release, triggering a Gill-type pattern over the western TP and generating anomalous anticyclonic circulation (Fig. 3; Gill 1980), this is consistent with the atmospheric response to an isolated equatorially asymmetric heating studied by Xing et al. (2014). Furthermore, the precipitation-induced ascending motion related to the IOT favors the enhanced descending motion over the western TP (Fig. 4). According to Zhang et al. (2022b), the lead-lag correlations that were calculated for the study period show that the IOT leads the southern tropical Asia

precipitation by one month. We also calculated the lead-lag correlations between the SAT over the western TP and the precipitation in the southern tropical Asia (Fig. 6c, d). Based on the results from both datasets, it is observed that the correlation coefficients between the precipitation in the southern tropical Asia and the SAT over the western TP reached the maximum value simultaneously, with the correlation coefficient exceeded 0.4 at > 95% confidence level. This means that when precipitation increases in southern tropical Asia, the SAT over the western TP rises simultaneously. Considering the relationship between the southern tropical Asia precipitation and the IOT, we hypothesize that establishing this indirect process between IOT and the SAT over the western TP likely takes about one month.

Previous studies have pointed out that Rossby waves are usually triggered when strong convection (rainfall) generates anomalous condensation latent heat, causing anomalous flow divergence and vorticity in the upper troposphere (Sardeshmukh and Hoskins 1988; Qin and Robinson 1993; Shi et al. 2024). Therefore, we calculated the RWS in Fig. 7a–d. As can be seen in the figure, the climatological RWS in the

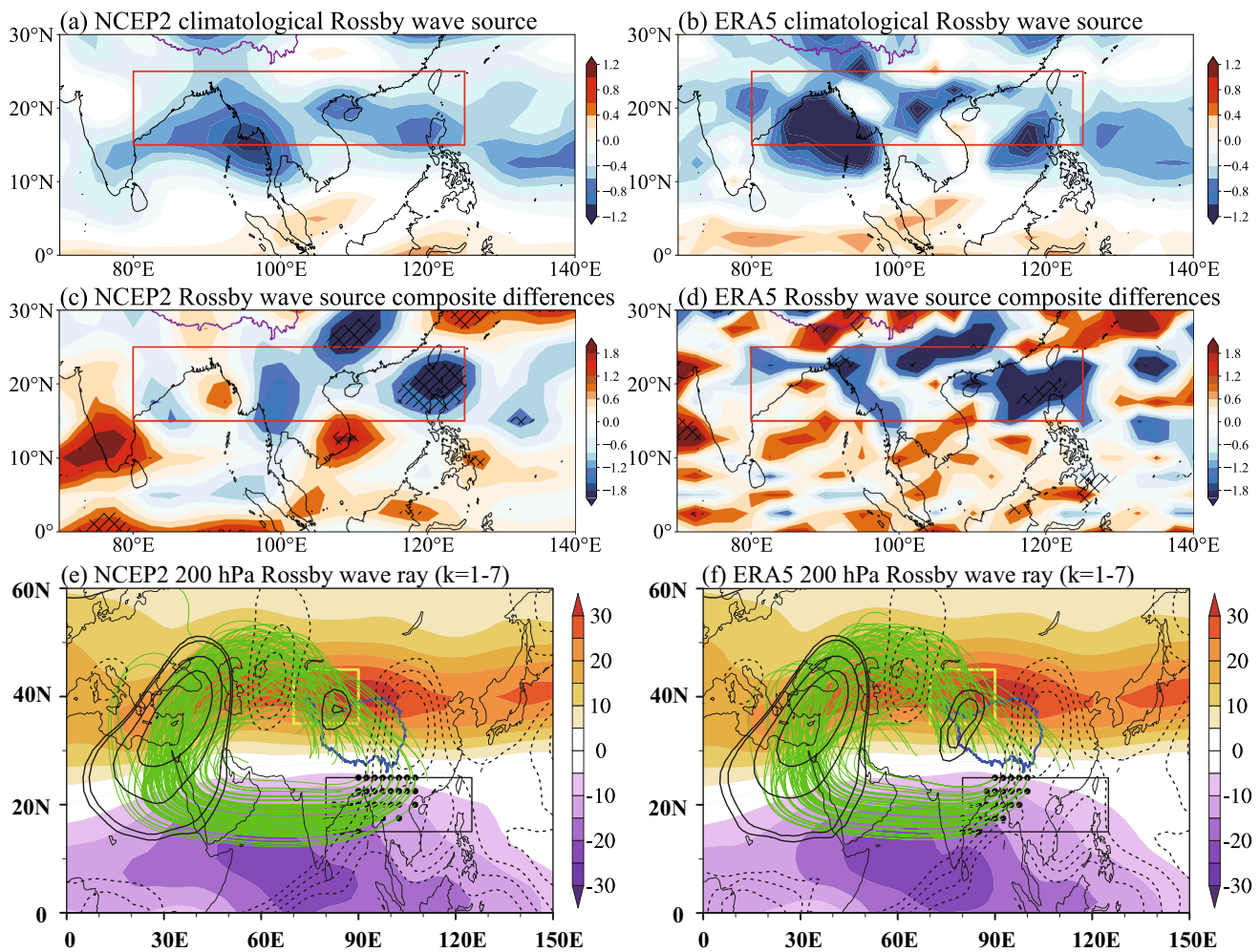


**Fig. 7** **a** Distribution of climatological JJA 200-hPa Rossby wave source ( $10^{-10} s^{-2}$ ) based on the NCEP2 dataset. **c** Composite differences map of the JJA 200-hPa Rossby wave source anomalies ( $10^{-9} s^{-2}$ ) between the positive IOT and negative IOT based on the NCEP2 dataset. The black slash areas indicate the significant values above the 90% confidence level. The red box in **(a)** and **(c)** denote the southern tropical Asia region. **e** Stationary Rossby wave trajectories at 200 hPa in a horizontally non-uniform climatological flow

(green curves) with zonal wavenumbers of 1–7 and the starting points of wave rays (black dots) in the southern tropical Asia region based on the NCEP2 dataset. The blue contour represents the outline of the TP. Shadings and contours are the climatological 200 hPa zonal and meridional winds ( $ms^{-1}$ ). The black and yellow boxes denote the southern tropical Asia and western TP regions, respectively. **b**, **d**, **f** As in **(a)**, **(c)**, **(e)**, but using the ERA5 dataset

southern tropical Asia is negative (Fig. 7a, b), which is consistent with previous results (Moon and Ha 2003; Lu and Baek-Jo 2004; Shimizu and Cavalcanti 2011; Ding et al. 2023). In addition, there are relatively significant negative composite differences in the southern tropical Asia (Fig. 7c, d). These mean that in the positive IOT phase, tropical southern Asia is conducive to Rossby wave excitation.

To further confirm the change of Rossby wave propagation from the southern tropical Asia, the Rossby wave ray is shown (e.g., Li and Li 2012; Li et al. 2015; Liu et al. 2018a, 2020; Zhang et al. 2022a, b). Figure 7e, f using the climatological wind from 1982 to 2022, illustrates the stationary Rossby wave trajectories in the horizontally non-uniform flow at 200 hPa when there is an increase

in latent heat release in the southern tropical Asia. It is worth noting that we firstly set the Rossby wave source throughout southern tropical Asia, and then selected the Rossby wave source whose Rossby wave rays can reach the western TP for mapping. The initial region of wave source in the southern tropical Asian region has a zonal wavenumber of 1–7. These initial signals first spread westward to the Red Sea, then north to western Russia at high altitudes (200 hPa) along the south and west side of the South Asian High, and finally east to the western TP (Fig. 7e, f), triggering a Gill-type response and resulting in anomalous anticyclonic circulation (Fig. 3). The research of Zhao et al. (2015, 2019) and Li et al. (2015) shows that meridional basic flow plays an important role

in promoting the propagation of stationary Rossby waves. In Fig. 7e, f, in the upper troposphere, westward climatological flows occur over the west of southern tropical Asia, which along with the anomalous easterly winds (Fig. 3), promotes the westward propagation of Rossby waves in the tropics. The prevailing southwesterly wind occur over the west of the prominent South Asian High, and along with the anomalous southwesterly winds (Fig. 3), they dominate the northward propagation of Rossby waves to higher latitudes. Upon reaching western Russia, the strong climatological westerly winds in the extratropical regions dominate the eastward transmission of Rossby waves to the western TP, and trigger a Gill-type response (Fig. 3). By calculating the correlation coefficient between IOT and the area-average geopotential height of the 200 hPa region over the western TP, we found that the two showed a significant positive correlation (not shown). Positive potential height anomalies usually correspond to anomalous anticyclones, which further confirms that when IOT is in positive phase, it is conducive to anomalous anticyclone formation over the western TP.

Consequently, the influence of the IOT on the circulation over the western TP region is indirect. The primary physical process involves the IOT first inducing cross-equatorial flow along the eastern coast off the coasts of East Africa and the western coast off the coasts of Sumatra/Java coasts, causing convergence of these two airflow branches in the southern tropical Asian region, resulting in upward motion and triggering anomalous precipitation, thus promoting latent heat release. The released-latent heat propagates the signal to the western TP through Rossby waves, and excites a Gill-type response here, thereby affecting the local circulation patterns.

## 5 Numerical experiments results

To examine the atmospheric response to the imposed positive IOT forcing (Fig. 8a), Fig. 8b shows the differences between the control simulation and the simulation with positive IOT forcing for precipitation and 850 hPa wind in JJA. In the central tropical Indian Ocean, a significant cyclonic circulation is observed, with significant anticyclonic circulations in the eastern and western tropical Indian Ocean. These two anticyclonic circulations converge in the southern tropical Asia region after crossing the equator. The precipitation field in the tropical Indian Ocean region exhibits a tripolar pattern, with a significant increase in precipitation in the central tropical Indian Ocean, and a significant decrease in precipitation in the eastern and western tropical Indian Ocean, which closely resembles the spatial structure of the IOT (Fig. 8b). These results are consistent with observations (Fig. 6a, b), and the surplus precipitation is reasonably reproduced over the southern tropical Asia region (Fig. 8b), again consistent with observations (Fig. 6a, b), albeit with a slight southward shift.

To verify the response of atmospheric circulation to the IOT forcing, Fig. 9a presents the geopotential height and wind at 200 hPa during JJA, based on differences between the control simulation and the simulation with positive IOT forcing. As seen in Fig. 9a, the positive geopotential height and anticyclonic anomalies are significant over the western TP. Moreover, in the simulation of omega, the simulated results effectively demonstrate the observed negative–positive–negative pattern from the subtropics to the higher latitudes, with significant anomalous subsidence over the western TP, which is crucial for warming. Despite the subsidence region over the western TP is shifted southward,

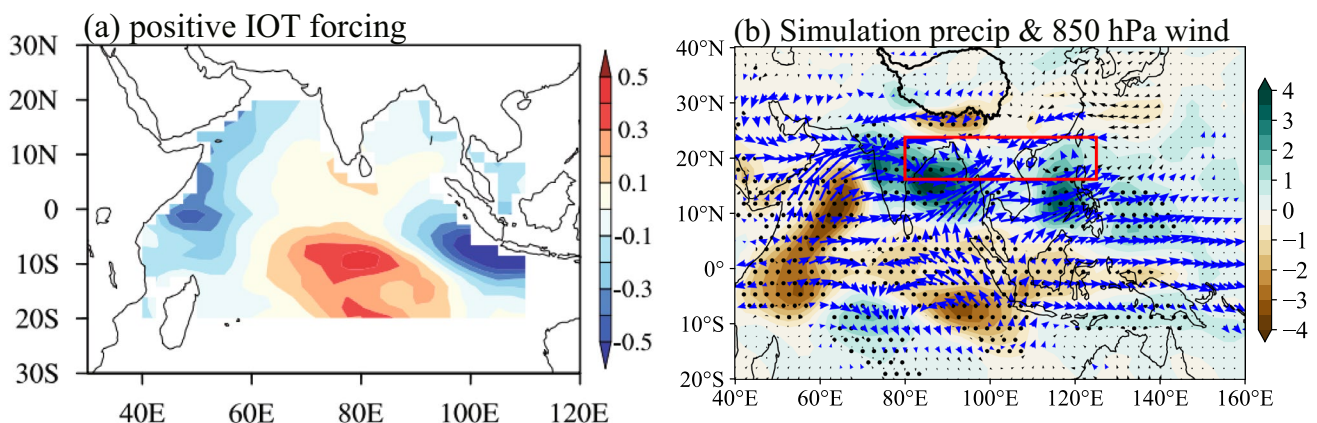
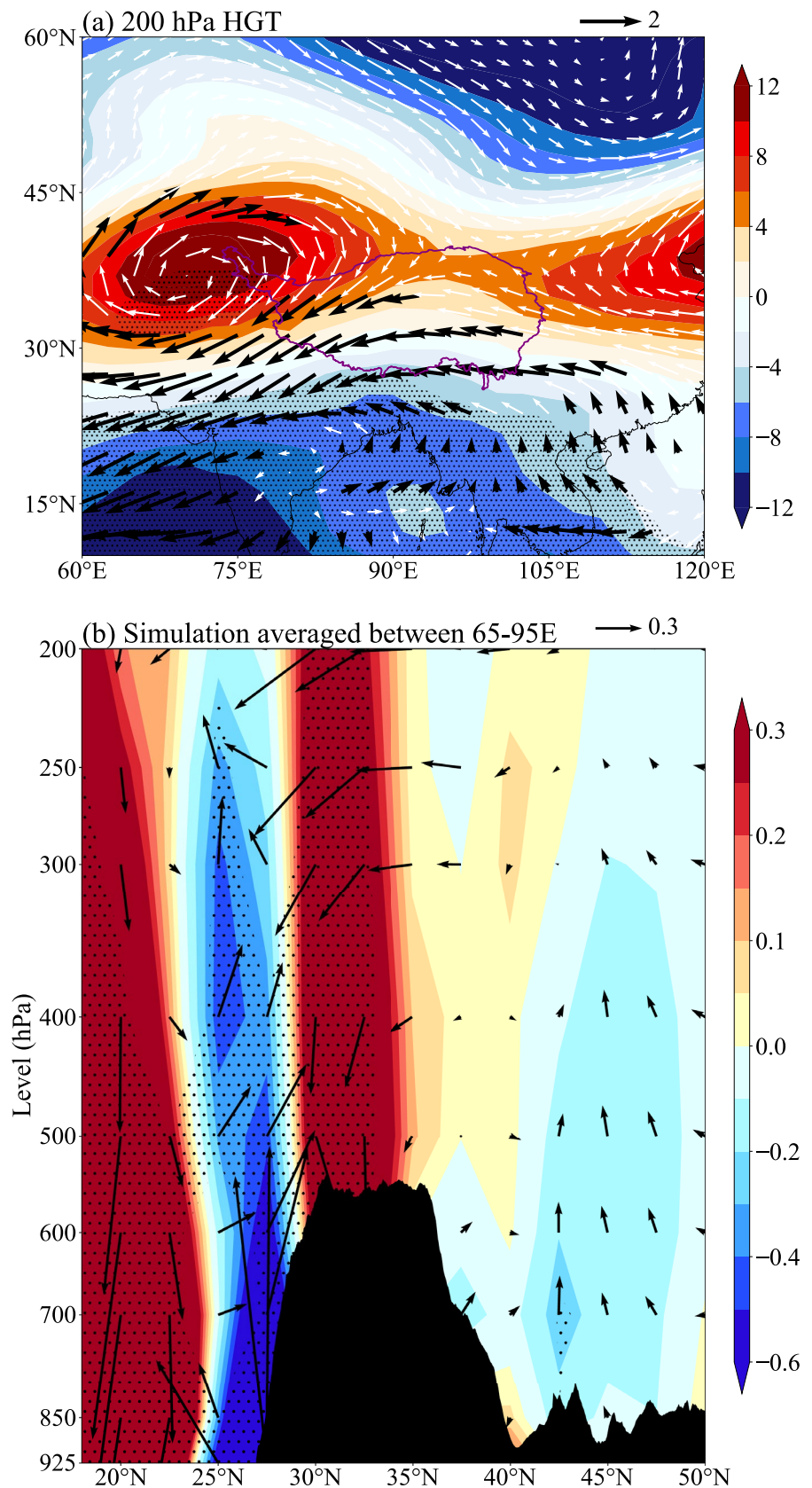


**Fig. 8** **a** Indian Ocean SSTA (shading, °C) that were used as the lower boundary conditions for the positive IOT forcing in CAM5 experiments. **b** Differences between the positive IOT forcing simulation and the control simulation for JJA mean precipitation (shading,

mm day<sup>-1</sup>) and 850 hPa wind (vector, m s<sup>-1</sup>). The black contour represents the outline of the TP. The red box denotes the southern tropical Asia region. The black vectors and the black stippled areas in (**b**) indicate significant values above the 95% confidence level



**Fig. 9** **a** Differences between the positive IOT forcing simulation and the control simulation for JJA mean geopotential height (shading, gpm) and wind (vector,  $\text{m s}^{-1}$ ) at 200 hPa. The purple contour represents the outline of the TP. The black vectors and the black stippled areas indicate significant values above the 90% confidence level. **b** As in (a), but for the mean meridional-vertical circulation (vectors,  $\text{m s}^{-1}$ ) and omega (shading,  $10^{-2} \text{ hPa s}^{-1}$ ) averaged over  $65^{\circ}$ – $95^{\circ}\text{E}$ . When plotting the shading, the negative values of omega were used





and there are some differences between the observations and simulations in the tropical regions (Fig. 9b). Overall, the anomalous atmospheric circulation conditions are consistent with the observations, indicating the prominent influence of the IOT on the atmospheric circulation over the western TP.

## 6 Discussion and summary

The IOT, as proposed by Zhang et al. (2020), represents a significant interannual variability of ocean–atmosphere coupling, exerting considerable influence on climate variability in the Northern Hemisphere and globally. This study focused on the impact of the IOT on SAT over the western TP during JJA and the underlying physical mechanisms.

Through observational data analysis, we found that during positive or negative phases of the IOT, SAT over the western TP during JJA respectively increased or decreased. The underlying physical processes may be summarized as follows. In the positive IOT events, anomalous cross-equatorial flows from both the tropical eastern and western Indian Ocean are induced. After crossing the equator, these flows converge over the southern tropical Asia, promoting localized precipitation increases. The surplus precipitation over the southern tropical Asia acts as a heat source, resulting in positive geopotential height anomalies and anomalous anticyclonic circulation over the western TP, based on the Gill-type response theory, accompanied by an anomalous sinking motion. Using Rossby wave ray tracing theory, we were able to demonstrate that anomalous precipitation over the southern tropical Asia excites a northward-propagating ACMT pattern, influencing the circulation over the western TP. The observed atmospheric circulation conditions were accurately reproduced using CAM5. Under such anomalous circulation patterns, an increase in atmospheric thickness through adiabatic processes ultimately leads to surface warming. Furthermore, anomalous circulation patterns may also affect SAT by influencing solar radiation influx over the western TP. The detailed physical processes through which the IOT influences SAT over the western TP during JJA are illustrated in Fig. 10.

In the CAM5 numerical model experiments, spatial differences were found between the results of anomalous SAT and observations (not shown). This was due mainly to the impact of the IOT first manifests in the southern tropical Asia region, where precipitation variations subsequently influenced the circulation over the western TP, thus affecting local SAT changes. The influence of the IOT on SAT over the western TP is thus indirect. Furthermore, the CAM5 numerical model experiments were able only to add a heat source over the ocean, whereas the direct influence on the western TP stems from increased latent heat release from the enhanced precipitation in the southern

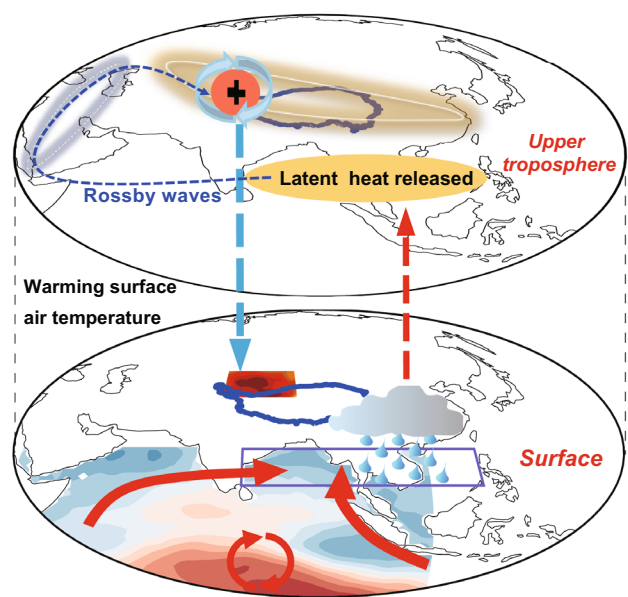


**Fig. 10** Schematic diagram illustrating the impact of the IOT on SAT over the western TP during JJA. Red (blue) shading and solid arrows represent positive (negative) SSTA and anomalous cross-equatorial winds over the tropical Indian Ocean during positive IOT events, respectively. The cloud with raindrops indicates positive precipitation anomalies over the southern tropical Asia region (light purple box) accompanied by latent heat release (yellow shading). Red (blue) dashed curves with arrows indicate upward (downward) motion anomalies. Light blue vectors represent anticyclonic circulation. Red circles denote positive anomalies in upper troposphere. The shaded white ellipses (solid or dashed) represent the climatological mean upper-level zonal (meridional) winds. The blue contour represents the outline of the TP

tropical Asia region. Hence, the coupled model applied in the future may overcome these limitations. CMIP6 models may also allow for the physical connection between the IOT and SAT over the western TP, which needs further in-depth study. In addition, we note that in Fig. 6a, b, significant westerly wind anomalies are observed east of the Philippines, where westerly winds are a key atmospheric factor for ENSO formation and development in the next season, suggesting that IOT may have some impact on subsequent ENSO formation and development, which needs further study in the future.

**Acknowledgements** Thanks for the Center for Taishan Pandeng Scholar Project, and High Performance Computing and System Simulation, Laoshan Laboratory (Qingdao) for providing computing resource.

**Author contributions** MZ and YZ contributed to the conceptualization and design of the study. Figures visualization and formal analysis were performed by MZ. MZ, YZ, and JL analyzed and interpreted the physical processes. The first draft of the manuscript was written by MZ, and all authors reviewed and approved the manuscript.

**Funding** This work was jointly sponsored by the National Natural Science Foundation of China (NSFC) Project (42130607; 42105055),

Laoshan Laboratory (No.LSKJ202202600); State Key Laboratory of Tropical Oceanography, South China Sea Institute of Oceanology, Chinese Academy of Sciences (LTO2309).

**Data availability** The monthly Optimum Interpolation SST (OISST) and extended Reconstructed SST version 5 (ERSST v5) datasets are both available at <https://psl.noaa.gov/data/gridded/tables/sst.html>. The monthly mean atmospheric variables were obtained from the National Centers for Environmental Prediction reanalysis 2 (NCEP2; <https://psl.noaa.gov/data/gridded/data.ncep.reanalysis2.html>) and the European Centre for Medium-Range Weather Forecasts (ECMWF) Reanalysis version 5 (ERA5; <https://www.ecmwf.int/en/forecasts/datasets/reanalysis-datasets/era5>). The two surface air temperature datasets were employed from the Global Historical Climatology Network (GHCN; <https://www.psl.noaa.gov/data/gridded/data.ghcncams.html>) and Berkeley Earth surface temperature (BEST; <https://berkeleyearth.org/data>). The precipitation datasets were derived from the Climate Prediction Center Merged Analysis of Precipitation (CMAP; <https://psl.noaa.gov/data/gridded/data.cmap.html>) and the Global Precipitation Climatology Project (GPCP; <https://psl.noaa.gov/data/gridded/data.gpcp.html>). Community Atmosphere Model Version 5 experiment outputs: <https://doi.org/https://doi.org/10.5281/zenodo.12567298>.

## Declarations

**Conflict of interest** The authors declare no competing interests.

## References

- Bafitlhile TM, Liu YB (2023) An asymmetric relationship between Tibetan Plateau surface temperature regimes and oceanic-atmospheric circulations. *Int J Climatol* 43(13):5884–5911. <https://doi.org/10.1002/joc.8179>
- Bretherton CS, Widmann M, Dymnikov VP, Wallace JM, Blade I (1999) The effective number of spatial degrees of freedom of a time-varying field. *J Clim* 12(7):1990–2009. [https://doi.org/10.1175/1520-0442\(1999\)012%3c1990:TENOSD%3e2.0.CO;2](https://doi.org/10.1175/1520-0442(1999)012%3c1990:TENOSD%3e2.0.CO;2)
- Cuo L, Zhang YX, Wang QC, Zhang LL, Zhou BR, Hao ZC, Su FG (2013) Climate change on the northern Tibetan Plateau during 1957–2009: Spatial patterns and possible mechanisms. *J Clim* 26(1):85–109. <https://doi.org/10.1175/JCLI-D-11-00738.1>
- Deng ZR, Zhou SW, Wang MR, He LQ, Qing YY, Qian ZT (2023) Variations in summer surface air temperature over the eastern Tibetan Plateau: connection with Barents–Kara spring sea ice and summer Arctic Oscillation. *J Geophys Res* 128(21):e2023JD039765. <https://doi.org/10.1029/2023JD039765>
- Deng ZR, Zhou SW, Ge XY, Qing YY, Yang C (2024) An interdecadal change in the relationship between summer Arctic Oscillation and surface air temperature over the eastern Tibetan Plateau around the late 1990s. *Clim Dyn* 62(1):87–101. <https://doi.org/10.1007/s00382-023-06899-0>
- Ding QH, Wang B (2005) Circumglobal teleconnection in the northern hemisphere summer. *J Clim* 18(17):3483–3505. <https://doi.org/10.1175/JCLI3473.1>
- Ding YH, Sun XT, Li QQ, Song YF (2023) Interdecadal variation in Rossby wave source over the Tibetan Plateau and its impact on the East Asia circulation pattern during boreal summer. *Atmosphere* 14(3):541. <https://doi.org/10.3390/atmos14030541>
- Du Y, Cai W, Wu Y (2013) A new type of the Indian Ocean Dipole since the mid-1970s. *J Clim* 26:959–972. <https://doi.org/10.1175/JCLI-D-12-00047.1>
- Endo S, Tozuka T (2016) Two flavors of the Indian Ocean dipole. *Clim Dyn* 46:3371–3385. <https://doi.org/10.1007/s00382-015-2773-0>
- Gill AE (1980) Some simple solutions for heat induced tropical circulation. *Q J R Meteor Soc* 106(449):447–462. <https://doi.org/10.1002/qj.49710644905>
- He ZQ, Wu R (2014) Indo-Pacific remote forcing in summer rainfall variability over the South China Sea. *Clim Dyn* 42:2323–2337. <https://doi.org/10.1007/s00382-014-2123-7>
- Hersbach H, Bell B, Berrisford P et al (2020) The ERA5 global reanalysis. *Quart J Roy Meteor Soc* 146(730):1999–2049. <https://doi.org/10.1002/qj.3803>
- Hoskins BJ, Karoly DJ (1981) The steady linear response of a spherical atmosphere to thermal and orographic forcing. *J Atmos Sci* 38:1179–1196. [https://doi.org/10.1175/1520-0469\(1981\)038%3c1179:TSLROA%3e2.0.CO;2](https://doi.org/10.1175/1520-0469(1981)038%3c1179:TSLROA%3e2.0.CO;2)
- Hu J, Duan AM (2015) Relative contributions of the Tibetan Plateau thermal forcing and the Indian Ocean Sea surface temperature basin mode to the interannual variability of the East Asian summer monsoon. *Clim Dyn* 45(9–10):2697–2711. <https://doi.org/10.1007/s00382-015-2503-7>
- Huang YF (2003) The relationship between the surface heating in Tibetan Plateau and spring air temperature in Sichuan-Chongqing area (in Chinese). *J Yunnan U* 25(5):428–433
- Huang BY, Thorne PW, Banzon VF, Boyer T, Zhang HM (2017) Extended reconstructed sea surface temperature, version 5 (ERSSTV5): Upgrades, validations, and intercomparisons. *J Clim* 30(20):8179–8205. <https://doi.org/10.1175/JCLI-D-16-0836.1>
- Huffman GJ, Bolvin DT, Nelkin EJ, Adler RF (2015) GPCP version 2.2 Combined Precipitation Data Set. Research Data Archive at the National Center for Atmospheric Research, Computational and Information Systems Laboratory. <https://doi.org/10.5065/D6R78C9S>
- Jiang XW, Zhang TT, Tam CY, Chen JW, Lau NC, Yang S, Wang ZY (2019) Impacts of ENSO and IOD on snow depth over the Tibetan Plateau: Roles of convections over the western North Pacific and Indian Ocean. *J Geophys Res* 124(22):11961–11975. <https://doi.org/10.1029/2019JD031384>
- Jiao Y, You QL, Lin HB, Min JZ (2014) The Arctic Oscillation effect on winter warming over the Tibetan Plateau (in Chinese). *J Glaciol Geocryol* 36(6):1385–1393
- Kanamitsu M, Ebisuzaki W, Woollen J, Yang S, Hnilo J, Fiorino M, Potter G (2002) NCEP-DOE AMIP-II reanalysis (R-2). *Bull Am Meteor Soc* 83(11):1631–1644. <https://doi.org/10.1175/BAMS-83-11-1631>
- Karoly DJ (1983) Rossby wave propagation in a barotropic atmosphere. *Dyn Atmos Oceans* 7:111–125. [https://doi.org/10.1016/0377-0265\(83\)90013-1](https://doi.org/10.1016/0377-0265(83)90013-1)
- Li YJ, Li JP (2012) Propagation of planetary waves in the horizontal non-uniform basic flow (in Chinese). *Chin J Geophys* 55:361–371. <https://doi.org/10.6038/j.issn.0001-5733.2012.02.001>
- Li L, Nathan TR (1997) Effects of low-frequency tropical forcing on intraseasonal tropical-extratropical interactions. *J Atmos Sci* 54:332–346. [https://doi.org/10.1175/1520-0469\(1997\)054%3c0332:EOLFTF%3e2.0.CO;2](https://doi.org/10.1175/1520-0469(1997)054%3c0332:EOLFTF%3e2.0.CO;2)
- Li L, Zhang RH (2021) Effect of upper-level air temperature changes over the Tibetan Plateau on the genesis frequency of Tibetan Plateau vortices at interannual timescales. *Clim Dyn* 57:341–352. <https://doi.org/10.1007/s00382-021-05715-x>
- Li L, Zhang RH (2023) Interdecadal shift in dipole pattern precipitation trends over the Tibetan Plateau: Roles of local vortices. *Geophys Res Lett* 50(5):e2022GL101445. <https://doi.org/10.1029/2022GL101445>
- Li J, Yu RC, Zhou TJ, Wang B (2005) Why is there an early spring cooling shift downstream of the Tibetan Plateau? *J Clim* 18(22):4660–4668. <https://doi.org/10.1175/JCLI3568.1>
- Li J, Yu RC, Zhou TJ (2008) Teleconnection between NAO and climate downstream of the Tibetan Plateau. *J Clim* 21(18):4680–4690. <https://doi.org/10.1175/2008JCLI2053.1>

- Li JP, Sun C, Jin FF (2013) NAO implicated as a predictor of Northern Hemisphere mean temperature multi-decadal variability. *Geophys Res Lett* 40(20):5497–5502. <https://doi.org/10.1002/2013GL057877>
- Li YJ, Li JP, Jin FF, Zhao S (2015) Interhemispheric propagation of stationary Rossby waves in a horizontally nonuniform background flow. *J Atmos Sci* 72(8):3233–3256. <https://doi.org/10.1175/JAS-D-14-0239.1>
- Li K, Liu XQ, Wang YB, Herzschuh U, Ni J, Liao MN, Xiao XY (2017) Late Holocene vegetation and climate change on the southeastern Tibetan Plateau: implications for the Indian Summer Monsoon and links to the Indian Ocean Dipole. *Quaternary Sci Rev* 177:235–245. <https://doi.org/10.1016/j.quascirev.2017.10.020>
- Li JP, Zheng F, Sun C, Feng J, Wang J (2019) Pathways of influence of the Northern Hemisphere mid–high latitudes on East Asian climate: a review. *Adv Atmos Sci* 36(9):902–921. <https://doi.org/10.1007/s00376-019-8236-5>
- Li JY, Li F, He SP, Wang HJ, Orsolini YJ (2021) The Atlantic multi-decadal variability phase dependence of teleconnection between the North Atlantic Oscillation in February and the Tibetan Plateau in March. *J Clim* 34(11):4227–4242. <https://doi.org/10.1175/JCLI-D-20-0157.1>
- Li JJ, Jin LY, Zheng ZY, Qin NS (2022a) Variability of the early summer temperature in the southeastern Tibetan Plateau in recent centuries and the linkage to the Indian Ocean basin mode. *Lithosphere-US* 1:9648384. <https://doi.org/10.2113/2022/9648384>
- Li JP, Xie TJ, Tang XX, Wang H, Sun C, Feng J, Zheng F, Ding RQ (2022b) Influence of the NAO on wintertime surface air temperature over East Asia: multidecadal variability and decadal prediction. *Adv Atmos Sci* 39(4):625–642. <https://doi.org/10.1007/s00376-021-1075-1>
- Liu T, Li JP, Li YJ, Zhao S, Zheng F, Zheng JY, Yao ZX (2018a) Influence of the may southern annular mode on the South China Sea summer Monsoon. *Clim Dyn* 51(11–12):4094–4107. <https://doi.org/10.1007/s00382-017-3753-3>
- Liu Y, Chen HP, Wang HJ, Qiu YB (2018b) The impact of the NAO on the delayed break-up date of lake ice over the southern Tibetan Plateau. *J Clim* 31(22):9073–9086. <https://doi.org/10.1175/JCLI-D-18-0197.1>
- Liu T, Li JP, Wang QY, Zhao S (2020) Influence of the autumn SST in the Southern Pacific Ocean on winter precipitation in the North American monsoon region. *Atmosphere* 11(8):844. <https://doi.org/10.3390/atmos11080844>
- Lu RY, Baek-Jo KIM (2004) The Climatological Rossby Wave Source over the STCZs in the Summer Northern Hemisphere. *J Meteorol Soc Japan Ser II* 82(2):657–669. <https://doi.org/10.2151/jmsj.2004.657>
- Meehl GA, Arblaster JM, Caron JM, Annamalai H, Jochum M, Chakraborty A, Murtugudde R (2012) Monsoon regimes and processes in CCSM4. Part I: The Asian-Australian monsoon. *J Clim* 25(8):2583–2608. <https://doi.org/10.1175/JCLI-D-11-00184.1>
- Menne MJ, Durre I, Vose RS, Gleason BE, Houston TG (2012) An overview of the global historical climatology network-daily database. *J Atmos Ocean Tech* 29(7):897–910. <https://doi.org/10.1175/JTECH-D-11-00103.1>
- Moon JY, Ha KJ (2003) Association between tropical convection and boreal wintertime extratropical circulation in 1982/83 and 1988/89. *Adv Atmos Sci* 20:593–603. <https://doi.org/10.1007/BF02915502>
- Qin JC, Robinson WA (1993) On the Rossby wave source and the steady linear response to tropical forcing. *J Atmos Sci* 50:1819–1823. [https://doi.org/10.1175/1520-0469\(1993\)050%3c1819:OTRWSA%3e2.0.CO;2](https://doi.org/10.1175/1520-0469(1993)050%3c1819:OTRWSA%3e2.0.CO;2)
- Reynolds RW, Rayner NA, Smith TM, Stokes DC, Wang W (2002) An improved in situ and satellite SST analysis for climate. *J Clim* 15(13):1609–1625. [https://doi.org/10.1175/1520-0442\(2002\)015%3c1609:AISAS%3e2.0.CO;2](https://doi.org/10.1175/1520-0442(2002)015%3c1609:AISAS%3e2.0.CO;2)
- Rohde R, Muller RA, Jacobsen R, Muller E, Perimutter S, Rosenfeld A, Wurtele J, Groom D, Wickham C (2013a) A new estimate of the average earth surface land temperature spanning 1753 to 2011. *Geoinfor Geostat* 1:1. <https://doi.org/10.4172/2327-4581.1000101>
- Rohde R, Muller RA, Jacobsen R, Perimutter S, Rosenfeld A, Wurtele J, Curry J, Wickham C, Mosher S (2013b) Berkeley earth temperature averaging process. *Geoinfor Geostat* 1(2):1–13. <https://doi.org/10.4172/2327-4581.1000103>
- Sardeshmukh PD, Hoskins BJ (1988) The generation of global rotational flow by steady idealized tropical divergence. *J Atmos Sci* 45:1228–1251. [https://doi.org/10.1175/1520-0469\(1988\)045%3c1228:TGOGRF%3e2.0.CO;2](https://doi.org/10.1175/1520-0469(1988)045%3c1228:TGOGRF%3e2.0.CO;2)
- Screen JA, Deser C, Simmonds I (2012) Local and remote controls on observed arctic warming. *Geophys Res Lett* 39(10):L10709. <https://doi.org/10.1029/2012GL051598>
- Shi J, Huang H, Fedorov AV et al (2024) Northeast Pacific warm blobs sustained via extratropical atmospheric teleconnections. *Nat Commun* 15:2832. <https://doi.org/10.1038/s41467-024-47032-x>
- Shimizu MH, Cavalcanti IF (2011) Variability patterns of Rossby wave source. *Clim Dyn* 37:441–454. <https://doi.org/10.1007/s00382-010-0841-z>
- Si YJ, Jin FM, Yang WC, Li Z (2023) Change and teleconnections of climate on the Tibetan Plateau. *Stoch Environ Res Risk Assess* 37(10):4013–4027. <https://doi.org/10.1007/s00477-023-02492-3>
- Son JH, Seo KH, Wang B (2020) How does the Tibetan Plateau dynamically affect downstream monsoon precipitation? *Geophys Res Lett* 47(23):e2020GL090543. <https://doi.org/10.1029/2020GL090543>
- Sun C, Li JP, Ding RQ (2016) Strengthening relationship between ENSO and Western Russian summer surface temperature. *Geophys Res Lett* 43(2):843–851. <https://doi.org/10.1002/2015GL067503>
- Tang QH, Zhang XJ, Yang XH, Francis JA (2013) Cold winter extremes in northern continents linked to arctic sea ice loss. *Environ Res Lett* 8(1):014036. <https://doi.org/10.1088/1748-9326/8/1/014036>
- Tao SY, Chen LS, Xu XD et al (1999) Progress of theoretical study in the second Tibetan plateau atmosphere scientific experiment (part I) (in Chinese). China Meteorological Press, Beijing, p 348
- Tozuka T, Endo S, Yamagata T (2016) Anomalous walker circulations associated with two flavors of the Indian Ocean dipole. *Geophys Res Lett* 44:5378. <https://doi.org/10.1002/2016GL068639>
- Wang YT, He Y, Hou SG (2007) Analysis of the temporal and spatial variations of snow cover over the Tibetan plateau based on MODIS (in Chinese). *J Glac Geocryol* 29(6):855–861
- Wang ZB, Wu RG, Chen SF, Huang G, Liu G, Zhu LH (2018) Influence of western Tibetan Plateau summer snow cover on East Asian summer rainfall. *J Geophys Res* 123(5):2371–2386. <https://doi.org/10.1002/2017jd028016>
- Wang H, Zheng F, Diao YN, Li JP, Sun RP, Tang XX, Sun Y, Li F, Zhang YZ (2022) The synergistic effect of the preceding winter Northern Hemisphere annular mode and spring tropical North Atlantic SST on spring extreme cold events in the mid-high latitudes of East Asia. *Clim Dyn* 59(11):3175–3191. <https://doi.org/10.1007/s00382-022-06237-w>
- Wang H, Li JP, Zheng F, Li F (2023) The synergistic effect of the summer NAO and northwest pacific SST on extreme heat events in the central–eastern China. *Clim Dyn* 61(9):4283–4300. <https://doi.org/10.1007/s00382-023-06807-6>
- Whitham G (1960) A note on group velocity. *J Fluid Mech* 9:347–352. <https://doi.org/10.1017/S0022112060001158>
- Xie PP, Arkin PA (1997) Global precipitation: A 17-year monthly analysis based on gauge observations, satellite estimates, and numerical model outputs. *Bull Amer Meteor Soc* 78(11):2539–2558.

- [https://doi.org/10.1175/1520-0477\(1997\)078%3c2539:GPAYMA%3e2.0.CO;2](https://doi.org/10.1175/1520-0477(1997)078%3c2539:GPAYMA%3e2.0.CO;2)
- Xing N, Li JP, Li YK (2014) Response of the tropical atmosphere to isolated equatorially asymmetric heating. *Chin J Atmos Sci (in Chinese)* 38(6):1147–1158. <https://doi.org/10.3878/j.issn.1006-9895.1401.13275>
- Yanai M, Li CF, Song ZS (1992) Seasonal heating of the Tibetan Plateau and its effects on the evolution of the Asian summer monsoon. *J Meteor Soc Japan* 70:319–351. [https://doi.org/10.2151/jmsj1965.70.1B\\_319](https://doi.org/10.2151/jmsj1965.70.1B_319)
- Ye DZ, Gao YX (1979) *Meteorology of the Qinghai-Xizang (Tibet) Plateau (in Chinese)*. Science Press, Beijing, p 278
- Yin ZY, Lin ZY, Zhao XY (2000) Temperature anomalies in central and eastern Tibetan Plateau in relation to general circulation patterns during 1951–1993. *Int J Climatol* 20(12):1431–1449. [https://doi.org/10.1002/1097-0088\(200010\)20:12%3c1431::AID-JOC551%3e3.0.CO;2-J](https://doi.org/10.1002/1097-0088(200010)20:12%3c1431::AID-JOC551%3e3.0.CO;2-J)
- Yong ZW, Wang ZG, Xiong JN, Ye CC, Sun HZ, Wu SJ (2023) Variability in temperature extremes across the Tibetan Plateau and its non-uniform responses to different ENSO types. *Clim Change* 176(7):91. <https://doi.org/10.1007/s10584-023-03566-5>
- Yu JH, Rong SY, Ren J (2005) The effects of Tibetan Plateau surface temperature on the precipitation over north China during rainy season (in Chinese). *Meteorol Sci Technol* 25:579
- Zhang P, Duan AM (2023) Precipitation anomaly over the Tibetan Plateau affected by tropical sea-surface temperatures and mid-latitude atmospheric circulation in September. *Sci China Earth Sci* 66:619–632. <https://doi.org/10.1007/s11430-022-1067-8>
- Zhang Y, Zhou W, Chow ECH, Leung MYT (2019) Delayed impacts of the IOD: cross-seasonal relationships between the IOD, Tibetan Plateau snow, and summer precipitation over the Yangtze-Huaihe River region. *Clim Dyn* 53:4077–4093. <https://doi.org/10.1007/s00382-019-04774-5>
- Zhang YZ, Li JP, Zhao S, Zheng F, Feng J, Li Y, Xu YD (2020) Indian Ocean tripole mode and its associated atmospheric and oceanic processes. *Clim Dyn* 55:1367–1383. <https://doi.org/10.1007/s00382-020-05331-1>
- Zhang P, Duan AM, Hu J (2022a) Combined effect of the tropical Indian Ocean and tropical North Atlantic sea surface temperature anomaly on the Tibetan Plateau precipitation anomaly in late summer. *J Clim* 35(22):7499–7518. <https://doi.org/10.1175/JCLI-D-21-0990.1>
- Zhang YZ, Li JP, Hou ZL, Zuo B, Xu YD, Tang XX, Wang H (2022b) Climatic effects of the Indian Ocean tripole on the Western United States in boreal summer. *J Clim* 35(8):2503–2523. <https://doi.org/10.1175/JCLI-D-21-0490.1>
- Zhang YZ, Li JP, Diao YN, Hou ZL, Liu T (2022c) Influence of the tropical Indian Ocean tripole on summertime cold extremes over Central Siberia. *Geophys Res Lett* 49:e2022GL100709. <https://doi.org/10.1029/2022GL100709>
- Zhao S, Li JP, Li Y (2015) Dynamics of an interhemispheric teleconnection across the critical latitude through a southerly duct during boreal winter. *J Clim* 28:7437–7456. <https://doi.org/10.1175/JCLI-D-14-00425.1>
- Zhao Y, Duan AM, Wu GX (2018) Interannual variability of late-spring circulation and diabatic heating over the Tibetan Plateau associated with Indian Ocean forcing. *Adv Atmos Sci* 35:927–941. <https://doi.org/10.1007/s00376-018-7217-4>
- Zhao S, Li JP, Li Y, Jin FF, Zheng J (2019) Interhemispheric influence of Indo-Pacific convection oscillation on Southern Hemisphere rainfall through southward propagation of Rossby waves. *Clim Dyn* 52:3203–3221. <https://doi.org/10.1007/s00382-018-4324-y>
- Zhou XJ, Zhao P, Chen JM, Chen LX, Li WL (2009) Impacts of thermodynamic processes over the Tibetan Plateau on the Northern Hemispheric climate. *Sci China Ser D-Earth Sci* 52:1679–1693. <https://doi.org/10.1007/s11430-009-0194-9>
- Zhou ZQ, Xie SP, Zhang R (2021) Historic Yangtze flooding of 2020 tied to extreme Indian Ocean conditions. *Proc Natl Acad Sci USA* 118(12):e2022255118. <https://doi.org/10.1073/pnas.2022255118>
- Zou H, Zhu JH, Zhou LB, Li P, Ma SP (2014) Validation and application of reanalysis temperature data over the Tibetan Plateau. *J Meteorol Res* 28(1):139–149. <https://doi.org/10.1007/s13351-014-3027-5>

**Publisher's Note** Springer Nature remains neutral with regard to jurisdictional claims in published maps and institutional affiliations.

Springer Nature or its licensor (e.g. a society or other partner) holds exclusive rights to this article under a publishing agreement with the author(s) or other rightsholder(s); author self-archiving of the accepted manuscript version of this article is solely governed by the terms of such publishing agreement and applicable law.